Nature Geoscience
May 2021, Volume 14 Issue 5 Pages 278-282
https://doi.org/10.1038/s41561-021-00716-1
https://archimer.ifremer.fr/doc/00882/99403/

Atlantic Equatorial Undercurrent intensification counteracts warming-induced deoxygenation

Brandt Peter [1, 2, *], Hahn Johannes [1], Schmidtko Sunke [1], Tuchen Franz Philip [1], Kopte Robert [3], Kiko Rainer [1, 4], Bourles Bernard [5], Czeschel Rena [1], Dengler Marcus [1]

[1] GEOMAR Helmholtz Centre for Ocean Research Kiel, Kiel, Germany
[2] Faculty of Mathematics and Natural Sciences, Kiel University, Kiel, Germany
[3] Institute of Geosciences, Kiel University, Kiel, Germany
[4] Laboratoire d'Océanographie de Villefranche, Sorbonne Université, Villefranche-sur-Mer, France
[5] Instrumentation, Moyens Analytiques, Observations en Géophysique et Océanographie, IRD, Plouzané, France

* Corresponding author : Peter Brandt, email address : pbrandt@geomar.de

Abstract :

The tropical Atlantic upper-ocean circulation experiences multiannual to decadal changes associated with different climate modes and is simultaneously adjusting to climate warming. The most energetic current in the tropical Atlantic is the Equatorial Undercurrent (EUC), which flows eastwards along the Equator. On the basis of long-term moored observations, we show that the EUC strengthened by more than 20% from 2008 to 2018. The intensification of the EUC is associated with increasing subsurface oxygen concentrations and a thickening of the upper-ocean oxygenated layer in the equatorial Atlantic. These changes counteract climate-warming-induced deoxygenation in the region. The EUC strengthening is found to be mainly forced by trade wind changes in the western tropical North Atlantic. A 60-yr dataset reveals that the recent oxygen increase in the upper equatorial Atlantic is associated with multidecadal variability. This variability is characterized by low oxygen concentrations in the 1990s and early 2000s, and high oxygen concentrations in the 1960s and 1970s. The observed oxygen variability seems to be linked to a compression and expansion of the habitat of tropical pelagic fish, and must be accounted for when evaluating the possible consequences of deoxygenation for marine ecosystems and fisheries. Recent strengthening of the Equatorial Undercurrent counteracts warming-induced deoxygenation in the equatorial Atlantic, according to an analysis of long-term moored observations.

Ocean circulation redistributes vast amounts of heat, freshwater and biogeochemical tracers, like nutrients and oxygen, throughout the climate system. It adjusts to climate warming, but at the same time varies with internal modes of natural climate variability. Suggested circulation changes due to climate warming include a strengthening of western boundary currents[1,2], a weakening of the Atlantic Meridional Overturning Circulation (AMOC)[3,4], or a general acceleration of the mean circulation[5]. Globally, the Atlantic Equatorial Undercurrent (EUC) is one of the most energetic currents. It transports thermocline waters eastward along the equator as part of the AMOC and the Subtropical Cells (STCs)[6]. The STCs represent shallow

overturning circulations involving subduction in the subtropics and upwelling at the equator[7,8]. The EUC strength is only weakly affected by prescribed AMOC changes as shown in forced simulations with constant wind forcing[9]. Instead, decadal variations of the Atlantic EUC detected in a 50-yr run of an assimilation model shows a close correspondence to the decadal variability of the STC strength[10]. Changes in the strength of the EUC may also result from a zonal redistribution of the equatorward pathways associated with the STCs within the thermocline, even without changing the STC strength, as found for the Pacific STCs in global warming simulations[11]. In a high-resolution forced ocean model, an STC weakening in the Pacific Ocean from the 1950s to the 2000s is associated with a weakening of the simulated EUC by 20%[12]. By keeping respiration constant in the model, a severe oxygen decline along the main STC thermocline pathways, including the EUC, is found. By implementing fully interactive biology, the effect of reduced ventilation on oxygen levels is, in turn, largely compensated by the effect of reduced productivity and associated oxygen consumption. A comparison with observed oxygen changes suggests, however, a likely overestimation of the biological effect in the model. The relative importance of the two competing effects remains unclear[12].

In the upper tropical Atlantic, moored observations have documented seasonal to multiannual variability of the North Brazil Undercurrent[13,14] and the EUC[15,16]. Circulation variability on decadal timescales, however, has not been detected in direct current observations so far. Nevertheless, decadal and multidecadal variability of oxygen concentration is well documented[17-20]. It is thought to mainly result from circulation changes that redistribute oxygen in the tropical oceans[21-24]. This oxygen variability is superimposed on the widespread deoxygenation as the global oceanic oxygen content is decreasing since the 1960s by more than 2%[25], thereby contributing to an expansion of the tropical oxygen minimum zones (OMZs). Both effects, internal oxygen variability and deoxygenation due to climate warming, must be accounted for when evaluating changes in low-oxygen regions and the longer-term impact of

these changes on marine ecosystems and fisheries[26], in particular the available habitat for tropical pelagic fish[27,28].

Strengthening of the Atlantic Equatorial Undercurrent

The velocity field of the EUC has been measured using direct current observations from a large number of research cruises crossing the equator at different longitudes[15,29,30]. Here, we focus on the central equatorial Atlantic at 23°W, where the EUC starts supplying the equatorial upwelling east of that longitude[15]. The EUC is located between 2°S and 1.5°N above a depth of 250 m. Its core is at about 80 m depth and is associated with an oxygen maximum with oxygen levels declining north- and southward from the core latitude close to the equator (Fig. 1b)[19]. Since December 2001, a long-term mooring has been operated almost continuously on the equator at 23°W (Fig. 1c, Supplementary Tab. 1)[31,32]. The mooring data have been used to derive an EUC transport time series starting in May 2005[16], here updated to September 2019 (Fig. 1a).

The most prominent signal in the EUC transport time series is a strengthening of the EUC from its lowest values in 2007 to its highest values in 2018 (Fig. 1a). We estimate a ten-year EUC transport increase from August 2008 to July 2018 of 3.3 ± 1.6 Sv decade^{-1}. This ten-year trend, which does not substantially change when shifting the examined ten-year period by a few years, corresponds to an increase of the EUC transport of more than 20% compared to its mean transport of about 14 Sv[16].

The time series of eastward velocity anomalies at the equator at 23°W shows an eastward velocity increase between about 70 m and 250 m. A maximum amplitude of nearly 0.2 m s^{-1} decade^{-1} at 100 m depth can be observed during the period from August 2008 to July 2018 (Fig. 1c, d). Above this layer, observed velocities become increasingly westward during the same period, with the ten-year trend reaching about –0.1 m s^{-1} decade^{-1}. Moored observations at the

equator at 10°W (Supplementary Fig. 1b) generally confirm the existence of a strengthening trend in the eastward velocity at thermocline level in the decade 2008-2018 (Supplementary Fig. 2).

Wind forcing of the circulation variability

The EUC is predominantly forced by the easterly wind along the equator that establishes an eastward pressure gradient with the sea level sloping downwards toward the east[33]. This local forcing results in an EUC transport variability in accordance with the dominantly multiannual variability of the Atlantic Niño, which is most pronounced in boreal summer[34,35]. Besides the local forcing, the EUC is also forced remotely by easterly winds in the tropics away from the equator driving poleward Ekman transport in both hemispheres. The resulting meridional Ekman transport divergence is directly related to the strength of the STCs and the EUC[8,10]. Typically, this Ekman divergence is quantified by the difference in the meridional Ekman transport across the latitudes 10°N and 10°S[8,36].

Meridional Ekman transports derived from different wind products consistently show an increase in the Ekman divergence between 10°N and 10°S for the decade 2008-2018 (Tab. 1, Fig. 1a, Supplementary Fig. 5). Since the westward wind stress at the equator shows no significant increase (Supplementary Tab. 3), it can be ruled out as a possible forcing of the EUC strengthening. The obtained ten-year trends in the Ekman divergence are, however, generally too small to account for the observed ten-year trend in the EUC transport. Nevertheless, it suggests a strengthening of the Atlantic STCs during the recent decade. Variations between the different wind products are substantial, but within the statistical uncertainties. All wind products suggest that the dominant forcing is in the northern hemisphere associated with a strengthening of the northeast trades (Tab. 1). Further analysis suggests that the wind changes occur dominantly in the western basins, with the eastern basins having only weak or even reversed ten-year trends (Supplementary Fig. 6, Supplementary Tab. 2).

Increased oxygenation of the upper equatorial Atlantic

The oxygen distribution along the equator (Fig. 2a) as measured during the recent cruise TRATLEQ 1 (Trans-Atlantic Equatorial cruise 1, Sep./Oct. 2019) is characterized by the presence of an OMZ in the eastern basin at mid-depth (lowest oxygen concentrations at about 400 m at 5°E off São Tomé). At the western boundary, the energetic North Brazil Current (NBC) transports high-oxygen waters northwestward. After crossing the equator, the NBC partly retroflects into the EUC contributing to the enhanced oxygen levels in the equatorial band[37]. The core of the EUC follows isopycnal surfaces shallowing from west to east (Fig. 2a, c). Water within the EUC core shows decreasing oxygen levels on its way toward the eastern boundary, mainly due to lateral eddy mixing with low-oxygen waters carried westward by the flows to the north and south of the EUC[19].

The measurements performed in Sep./Oct. 2019 show a specific pattern of elevated oxygen levels with respect to the climatological state of the oxygen distribution estimated for the year 2000 as taken from[25] (Fig. 2b, see [25] for details). The largest oxygen increase of more than 20 μmol kg^{-1} is found in the upper 250 m east of 10°W. Generally, enhanced oxygen levels in Sep./Oct. 2019 are found along the whole path of the EUC toward the eastern boundary as well as within the NBC close to the western boundary. The high oxygen levels thus represent a continuation of an oxygenation in the upper equatorial Atlantic estimated for the period 2006-2018 using oxygen data from a large number of research cruises along 23°W in the central equatorial Atlantic (Supplementary Fig. 10a).

The upper-ocean oxygen changes correspond to changes in the thickness of the uppermost oxygenated layer. Here, we define the oxygenated layer thickness (OLT) to be the depth range between the ocean surface and the shallowest depth of the 120 μmol kg^{-1} oxygen surface. While the chosen oxygen level is relatively high with respect to intermediate hypoxias defined elsewhere[38], it is suitable to describe long-term changes in the near-surface habitat of tropical

pelagic fish[28,39]. The mean OLT in the tropical Atlantic shows a characteristic pattern having small values above the OMZs of the eastern tropical North and South Atlantic and slightly larger values along the equator. At the western boundary and in the subtropics poleward of the OMZs, an extensive oxygenated layer is present (Fig. 3a). Using a comprehensive 60-year oxygen dataset, we provide evidence that the equatorial Atlantic undergoes a substantial multidecadal variability with a particularly large OLT in the 1960s and 1970s and a reduced OLT in the 1990s and 2000s (Fig. 3b). Since approximately 2005, a deepening of the 120 μmol kg^{-1} oxygen surface is observed with largest OLTs occurring in Sep./Oct. 2019. This multidecadal variability that is similarly seen in the subsurface oxygen levels (Fig. 3c) dominates any long-term changes that might be present[28] and clearly affects trends in the OLT calculated for different time spans, e.g. over the periods 1960-2005 or 1960-2020 (Supplementary Fig. 9).

Mechanisms of equatorial Atlantic oxygen variability

The global oceanic oxygen content has declined since the 1960s by about 2%[25] with notable deoxygenation occurring in the upper tropical ocean (Supplementary Fig. 8). About half of the deoxygenation in the upper 1000 m is suggested to be the result of changing oxygen solubility due to warming waters[25]. In general, the vertical structure of warming-induced oxygen changes might be more complicated as other effects like increased stratification or poleward migration of outcropping density surfaces might come into play[24] (see supplementary information). Additionally, the deoxygenation pattern associated with a warming ocean is superimposed by ocean variability on different timescales related to the internal variability of the climate system[12,23,40]. Oxygen observations during the last decades reveal substantial variability in the tropical Atlantic on multiannual to decadal timescales[19,23]. However, large uncertainty exists regarding the mechanisms of decadal oxygen changes. Observed oxygen trends calculated over the last 50 years are largely not in agreement with oxygen trends diagnosed from

biogeochemical model runs[41]. Depending on the specific model used, projections of subsurface oxygen levels also deviate[42]. The here reported strengthening of the Atlantic STCs and EUC in the decade 2008-2018 in response to an increased Ekman divergence between 10°N and 10°S (Fig. 1a) add a so far undescribed mechanism for decadal subsurface oxygen variability in the equatorial Atlantic. The vertical structure of the ten-year velocity trend at the equator at 23°W (Fig. 1d) shows that the strengthening of the EUC is associated with an intensifying near-surface westward flow. The intensified westward flow balances the increased Ekman divergence predominantly occurring in the western basin (Supplementary Fig. 6, Supplementary Tab. 2). Other mechanisms, such as changing STC pathways[11], may also contribute to the observed strengthening of the EUC at 23°W.

Here we have shown that the observed strengthening of the EUC is associated with a substantial oxygen increase in the upper equatorial Atlantic (Fig. 2b, Fig. 3c, Supplementary Fig. 10). A quantification of the link between EUC intensification and subsurface oxygenation can be made by the evaluation of the oxygen budget of a subsurface volume (see methods). Estimating the flushing time of a subsurface box (100-200 m, 4°S-4°N, 35°W-5°W) by the intensifying EUC yields a timescale similar to the here reported ten-year period of EUC intensification (Supplementary Fig. 4). This short flushing timescale substantiates the dominant role of the advective oxygen supply by the EUC to the oxygen budget. However, negative feedback mechanisms might dampen the oxygen response to the intensifying inflow of oxygenated EUC waters. These mechanisms may include an oxygen reduction due to changing advection (mean and eddy advection) as well as vertical mixing in response to increasing subsurface oxygen levels. As indicated by model studies, part of the enhanced ventilation might also be compensated by enhanced primary productivity and enhanced oxygen consumption[12]. So far, enhanced productivity in the equatorial Atlantic is not observed[43]. This could indicate that a possible compensation effect due to enhanced productivity is not of the same order as the

enhanced ventilation. For the eastern tropical North Pacific away from the equator, changes in the biological productivity forced by the trade winds are instead suggested to be responsible for decadal to centennial oxygen changes[40]. According to that mechanism, enhanced trade winds force a shallowing of the thermocline that results in enhanced primary production and respiration and consequently leads to reduced oxygen levels in the thermocline. Such behavior resulting from a similar forcing, i.e. the strengthening or weakening of the trade winds, would imply opposing oxygen changes in different parts of the tropical oceans.

The variability of the northeast trade winds is likely linked to the Atlantic Multidecadal Variability (AMV) changing from its cold phase in the 1970s to its warm phase in the 2000s followed by another cold phase[44-46]. The AMV affects the trade winds in the northern hemisphere, which are weakest during its warm phase[47,48]. While all analyzed wind products generally confirm a strengthening of the Ekman divergence in the decade 2008-2018 (mostly due to the increase in northern hemisphere Ekman transport), its magnitude varies by almost a factor of two (Tab. 1). Similar uncertainties in wind trends for specific periods were obtained when analyzing different reanalysis products[49]. For some wind products it is explicitly stated that they are not well suited for studies of long-term wind trends (e.g. https://climatedataguide.ucar.edu/climate-data/ccmp-cross-calibrated-multi-platform-wind-vector-analysis). Despite the uncertainties in multidecadal wind variability, equatorial oxygen observations reveal a multidecadal cycle of deoxygenation and oxygenation in the equatorial Atlantic (Fig. 3). This cycle is possibly linked to the AMV via its effect on the STCs. This internal variability of the climate system likely impacts marine ecosystems and fisheries in the equatorial Atlantic by compressing and expanding the habitat of tropical pelagic fish[28,50] on decadal timescales. A better understanding and prediction of locally amplified internal variability, as observed in the equatorial Atlantic, is crucial in order to improve the performance of forced ocean biogeochemistry circulation models. Furthermore, it substantially aids the

evaluation of impacts of climate change induced global deoxygenation on the marine ecosystem and its socioeconomic dependencies.

References

1 Yang, H. *et al.* Intensification and poleward shift of subtropical western boundary currents in a warming climate. *J Geophys Res-Oceans* **121**, 4928-4945, doi:10.1002/2015jc011513 (2016).

2 Todd, R. E. *et al.* Global Perspectives on Observing Ocean Boundary Current Systems. *Front Mar Sci* **6**, doi:10.3389/fmars.2019.00423 (2019).

3 Rahmstorf, S. *et al.* Exceptional twentieth-century slowdown in Atlantic Ocean overturning circulation. *Nat Clim Change* **5**, 475-480, doi:10.1038/Nclimate2554 (2015).

4 Frajka-Williams, E. *et al.* Atlantic Meridional Overturning Circulation: Observed Transport and Variability. *Front Mar Sci* **6**, doi:10.3389/fmars.2019.00260 (2019).

5 Hu, S. J. *et al.* Deep-reaching acceleration of global mean ocean circulation over the past two decades. *Sci Adv* **6**, doi:10.1126/sciadv.aax7727 (2020).

6 Hazeleger, W. & Drijfhout, S. Subtropical cells and meridional overturning circulation pathways in the tropical Atlantic. *J Geophys Res-Oceans* **111**, doi:10.1029/2005jc002942 (2006).

7 Zhang, D. X., McPhaden, M. J. & Johns, W. E. Observational evidence for flow between the subtropical and tropical Atlantic: The Atlantic subtropical cells. *J Phys Oceanogr* **33**, 1783-1797, doi:10.1175/2408.1 (2003).

8 Schott, F. A., McCreary, J. P. & Johnson, G. C. in *Earth Climate: The Ocean-Atmosphere Interaction Geophysical Monograph 147* (eds C. Wang, S.-P. Xie, & J. A. Carton) 261-304 (American Geophysical Union, 2004).

9 Fratantoni, D. M., Johns, W. E., Townsend, T. L. & Hurlburt, H. E. Low-latitude circulation and mass transport pathways in a model of the tropical Atlantic ocean. *J Phys Oceanogr* **30**, 1944-1966, doi:Doi 10.1175/1520-0485(2000)030<1944:Llcamt>2.0.Co;2 (2000).

10 Rabe, B., Schott, F. A. & Kohl, A. Mean circulation and variability of the tropical Atlantic during 1952-2001 in the GECCO assimilation fields. *J Phys Oceanogr* **38**, 177-192, doi:10.1175/2007jpo3541.1 (2008).

11 Luo, Y. Y., Rothstein, L. M. & Zhang, R. H. Response of Pacific subtropical-tropical thermocline water pathways and transports to global warming. *Geophys Res Lett* **36**, doi:10.1029/2008gl036705 (2009).

12 Duteil, O., Böning, C. W. & Oschlies, A. Variability in subtropical-tropical cells drives oxygen levels in the tropical Pacific Ocean. *Geophys Res Lett* **41**, 8926-8934, doi:10.1002/2014gl061774 (2014).

13 Schott, F. A. *et al.* The shallow and deep western boundary circulation of the South Atlantic at 5°-11°S. *J Phys Oceanogr* **35**, 2031-2053, doi:doi:10.1175/JPO2813.1 (2005).

14 Hummels, R. *et al.* Interannual to decadal changes in the western boundary circulation in the Atlantic at 11 degrees S. *Geophys Res Lett* **42**, 7615-7622, doi:10.1002/2015gl065254 (2015).

15 Johns, W. E. *et al.* Zonal structure and seasonal variability of the Atlantic Equatorial Undercurrent. *Clim Dynam* **43**, 3047-3069, doi:10.1007/s00382-014-2136-2 (2014).

16 Brandt, P., Funk, A., Tantet, A., Johns, W. & Fischer, J. The Equatorial Undercurrent in the central Atlantic and its relation to tropical Atlantic variability. *Clim Dynam* **43**, 2985-2997, doi:10.1007/s00382-014-2061-4 (2014).

17 Stramma, L., Johnson, G. C., Sprintall, J. & Mohrholz, V. Expanding oxygen-minimum zones in the tropical oceans. *Science* **320**, 655-658, doi:10.1126/Science.1153847 (2008).

18 Deutsch, C., Brix, H., Ito, T., Frenzel, H. & Thompson, L. Climate-Forced Variability of Ocean Hypoxia. *Science* **333**, 336-339, doi:10.1126/Science.1202422 (2011).

19 Brandt, P. *et al.* On the role of circulation and mixing in the ventilation of oxygen minimum zones with a focus on the eastern tropical North Atlantic. *Biogeosciences* **12**, 489-512, doi:10.5194/bg-12-489-2015 (2015).

20 Montes, E. *et al.* Decadal variability in the oxygen inventory of North Atlantic subtropical underwater captured by sustained, long-term oceanographic time series observations. *Global Biogeochem Cy* **30**, 460-478, doi:10.1002/2015gb005183 (2016).

21 Ito, T. & Deutsch, C. Variability of the oxygen minimum zone in the tropical North Pacific during the late twentieth century. *Global Biogeochem Cy* **27**, 1119-1128, doi:10.1002/2013gb004567 (2013).

22 Duteil, O., Schwarzkopf, F. U., Böning, C. W. & Oschlies, A. Major role of the equatorial current system in setting oxygen levels in the eastern tropical Atlantic Ocean: A high- resolution model study. *Geophys Res Lett* **41**, 2033-2040, doi:doi:10.1002/2013gl058888 (2014).

23 Hahn, J., Brandt, P., Schmidtko, S. & Krahmann, G. Decadal oxygen change in the eastern tropical North Atlantic. *Ocean Sci* **13**, 551-576, doi:10.5194/os-13-551-2017 (2017).

24 Oschlies, A., Brandt, P., Stramma, L. & Schmidtko, S. Drivers and mechanisms of ocean deoxygenation. *Nat Geosci* **11**, 467-473, doi:10.1038/s41561-018-0152-2 (2018).

25 Schmidtko, S., Stramma, L. & Visbeck, M. Decline in global oceanic oxygen content during the past five decades. *Nature* **542**, 335-339, doi:10.1038/nature21399 (2017).

26 Breitburg, D. *et al.* Declining oxygen in the global ocean and coastal waters. *Science* **359**, doi:10.1126/science.aam7240 (2018).

27 Leung, S., Thompson, L., McPhaden, M. J. & Mislan, K. A. S. ENSO drives near-surface oxygen and vertical habitat variability in the tropical Pacific. *Environ Res Lett* **14**, doi:10.1088/1748-9326/ab1c13 (2019).

28 Stramma, L. *et al.* Expansion of oxygen minimum zones may reduce available habitat for tropical pelagic fishes. *Nat Clim Change* **2**, 33-37, doi:10.1038/Nclimate1304 (2012).

29 Schott, F. A. *et al.* The zonal currents and transports at 35 degrees W in the tropical Atlantic. *Geophys Res Lett* **30**, doi:10.1029/2002gl016849 (2003).

30 Kolodziejczyk, N., Bourlès, B., Marin, F., Grelet, J. & Chuchla, R. Seasonal variability of the Equatorial Undercurrent at 10 degrees W as inferred from recent in situ observations. *J Geophys Res-Oceans* **114**, doi:10.1029/2008JC004976 (2009).

31 Bourlès, B. *et al.* PIRATA: A Sustained Observing System for Tropical Atlantic Climate Research and Forecasting. *Earth Space Sci* **6**, 577-616, doi:10.1029/2018ea000428 (2019).

32 Foltz, G. R. *et al.* The Tropical Atlantic Observing System. *Front Mar Sci* **6**, doi:10.3389/fmars.2019.00206 (2019).

33 Wacongne, S. Dynamical regimes of a fully nonlinear stratified model of the Atlantic Equatorial Undercurrent. *J Geophys Res-Oceans* **94**, 4801-4815, doi:doi:10.1029/JC094iC04p04801 (1989).

34 Chang, P. *et al.* Climate fluctuations of tropical coupled systems - The role of ocean dynamics. *J Climate* **19**, 5122-5174, doi:10.1175/Jcli3903.1 (2006).

35 Hormann, V. & Brandt, P. Atlantic Equatorial Undercurrent and associated cold tongue variability. *J Geophys Res-Oceans* **112**, doi:10.1029/2006jc003931 (2007).

36 Tuchen, F. P., Lübbecke, J. F., Schmidtko, S., Hummels, R. & Böning, C. W. The Atlantic Subtropical Cells Inferred from Observations. *J Geophys Res-Oceans*, doi:10.1029/2019jc015396 (2019).

37 Schott, F. A., Fischer, J. & Stramma, L. Transports and pathways of the upper-layer circulation in the western tropical Atlantic. *J Phys Oceanogr* **28**, 1904-1928, doi:10.1175/1520-0485(1998)028<1904:TAPOTU>2.0.CO;2 (1998).

38 Levin, L. A. Manifestation, Drivers, and Emergence of Open Ocean Deoxygenation. *Annual Review of Marine Science, Vol 10* **10**, 229-260, doi:10.1146/annurev-marine-121916-063359 (2018).

39 Vaquer-Sunyer, R. & Duarte, C. M. Thresholds of hypoxia for marine biodiversity. *P Natl Acad Sci USA* **105**, 15452-15457, doi:10.1073/pnas.0803833105 (2008).

40 Deutsch, C. *et al.* Centennial changes in North Pacific anoxia linked to tropical trade winds. *Science* **345**, 665-668, doi:10.1126/Science.1252332 (2014).

41 Stramma, L., Oschlies, A. & Schmidtko, S. Mismatch between observed and modeled trends in dissolved upper-ocean oxygen over the last 50 yr. *Biogeosciences* **9**, 4045-4057, doi:10.5194/Bg-9-4045-2012 (2012).

42 Bopp, L. *et al.* Multiple stressors of ocean ecosystems in the 21st century: projections with CMIP5 models. *Biogeosciences* **10**, 6225-6245, doi:10.5194/bg-10-6225-2013 (2013).

43 Rousseaux, C. S. & Gregg, W. W. Recent decadal trends in global phytoplankton composition. *Global Biogeochem Cy* **29**, 1674-1688, doi:10.1002/2015gb005139 (2015).

44 Zhang, R. & Delworth, T. L. Simulated tropical response to a substantial weakening of the Atlantic thermohaline circulation. *J Climate* **18**, 1853-1860, doi:Doi 10.1175/Jcli3460.1 (2005).

45 Knight, J. R., Folland, C. K. & Scaife, A. A. Climate impacts of the Atlantic Multidecadal Oscillation. *Geophys Res Lett* **33**, doi:10.1029/2006gl026242 (2006).

46 Frajka-Williams, E., Beaulieu, C. & Duchez, A. Emerging negative Atlantic Multidecadal Oscillation index in spite of warm subtropics. *Sci Rep-Uk* **7**, doi:10.1038/s41598-017-11046-x (2017).
47 Delworth, T. L. & Mann, M. E. Observed and simulated multidecadal variability in the Northern Hemisphere. *Clim Dynam* **16**, 661-676, doi:DOI 10.1007/s003820000075 (2000).
48 Yuan, T. L. *et al.* Positive low cloud and dust feedbacks amplify tropical North Atlantic Multidecadal Oscillation. *Geophys Res Lett* **43**, 1349-1356, doi:10.1002/2016gl067679 (2016).
49 Ramon, J., Lledó, L., Torralba, V., Soret, A. & Doblas-Reyes, F. J. What global reanalysis best represents near-surface winds? *Q J Roy Meteor Soc* **145**, 3236-3251, doi:10.1002/qj.3616 (2019).
50 Hollowed, A. B. *et al.* Projected impacts of climate change on marine fish and fisheries. *Ices J Mar Sci* **70**, 1023-1037, doi:10.1093/icesjms/fst081 (2013).

Corresponding author

Peter Brandt, GEOMAR Helmholtz-Zentrum für Ozeanforschung Kiel, Düsternbrooker Weg 20, D-24105 Kiel, Germany, E-mail: pbrandt@geomar.de, Tel.: +49 431 600 4105, Fax: +49 431 600 4102

Author Information

Reprints and permissions information is available at www.nature.com/reprints. The authors declare no competing financial interests. Readers are welcome to comment on the online version of the paper. Correspondence and requests for materials should be addressed to P.B. (pbrandt@geomar.de).

Acknowledgments This study was funded by EU H2020 under grant agreement 817578 TRIATLAS project, by the Deutsche Forschungsgemeinschaft as part of the Sonderforschungsbereich 754 ‘‘Climate–Biogeochemistry Interactions in the Tropical Ocean’’ and through several research cruises with RV Meteor and RV Maria S. Merian and by the Deutsche Bundesministerium für Bildung und Forschung (BMBF) as part of the projects NORDATLANTIK (03F0443B) and RACE-Synthese (03F0824C). R.Ki. was additionally supported by a Make Our Planet Great Again grant of the French Agence Nationale de la Recherche under the “Programme d’Investissements d’Avenir”, reference ANR-19-MPGA-0012. We thank the captains, crews, scientists, and technical groups involved in the different national and international research cruises to the tropical Atlantic that contributed to collecting shipboard and mooring data, and making them freely available. Part of the velocity and oxygen observations were acquired within the PIRATA project and the CLIVAR TACE program. We would like to thank Dongxiao Zhang and Richard Greatbatch for helpful comments.

Author contributions P.B. designed the long-term measurement program, supervised the data analysis and wrote the first version of the manuscript; J.H. analyzed shipboard sections along

23°W, S.S. analyzed historical and recent oxygen data, F.P.T. analyzed moored velocity data, R.Ko., F.P.T., J.H. calculated and analyzed EUC transport time series, J.H., F.P.T. analyzed different wind products, R.Ki., B.B., R.C, M.D. contributed additional data and expertise on equatorial ocean dynamics and oxygen changes. All authors discussed the results and wrote the manuscript.

382 **Tab. 1** Ten-year (August 2008 to July 2018) trend in Ekman divergence (10°N-10°S),
383 northward Ekman transport at 10°N, and southward Ekman transport at 10°S with 95%
384 confidence interval for different wind products.

Wind Product	Ekman Divergence (10°N – 10°S) [Sv decade^{-1}]	Northward Ekman Transport across 10°N [Sv decade^{-1}]	Southward Ekman Transport across 10°S [Sv decade^{-1}]
ASCAT	2.0 ± 1.2	1.5 ± 1.2	0.4 ± 0.6
CCMP	1.1 ± 1.2	1.0 ± 1.1	0.1 ± 0.6
JRA55-do	1.5 ± 1.0	1.3 ± 1.0	0.2 ± 0.7

385

386

Figure captions

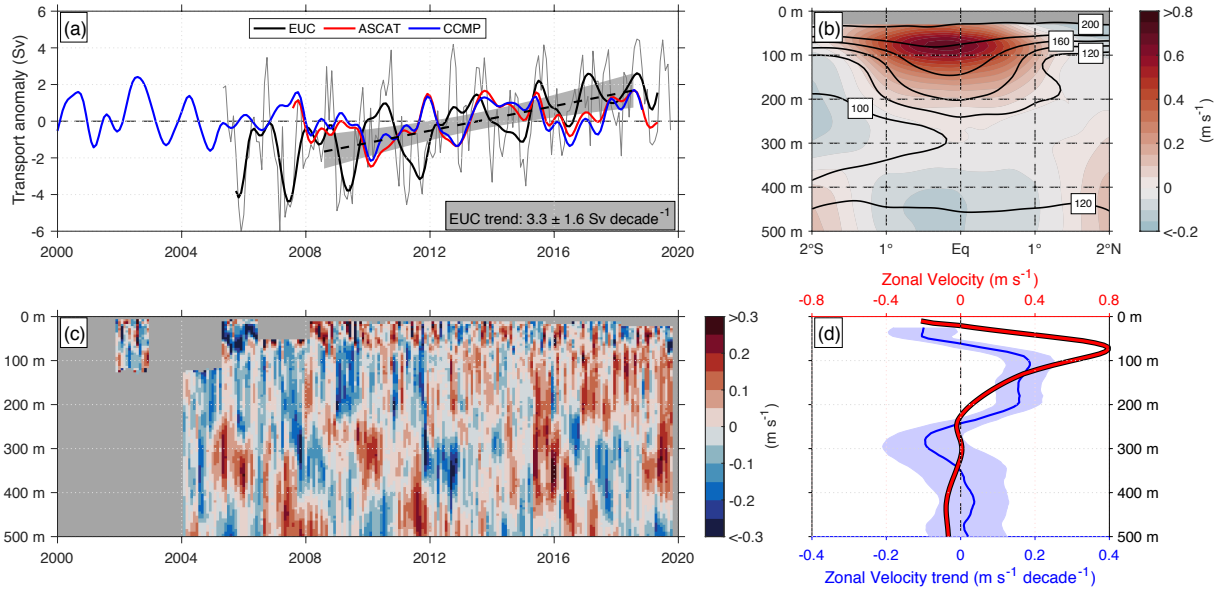

Fig. 1 The Atlantic Equatorial Undercurrent (EUC) at 23°W. a, EUC transport anomaly (monthly data, grey thin line; mean and annual and semi-annual harmonics subtracted and 270-day low-pass filtered, black thick line; ten-year (August 2008 to July 2018) trend, black dashed line; with 95% confidence interval, grey shading) and STC transport anomaly calculated from Ekman divergence between 10°N and 10°S using different wind forcing products (ASCAT, red; CCMP, blue; mean and annual and semi-annual harmonics subtracted and 270-day low-pass filtered). **b**, Mean eastward velocity (color) and dissolved oxygen (μmol kg^{-1}, contours) from shipboard measurements after[19]. **c**, Time series of eastward velocity anomaly at the equator with mean and seasonal cycle subtracted. **d**, Ten-year (August 2008 to July 2018) trend in eastward velocity (blue, with 95% confidence interval, light blue shading) and mean eastward velocity (red) at the equator.

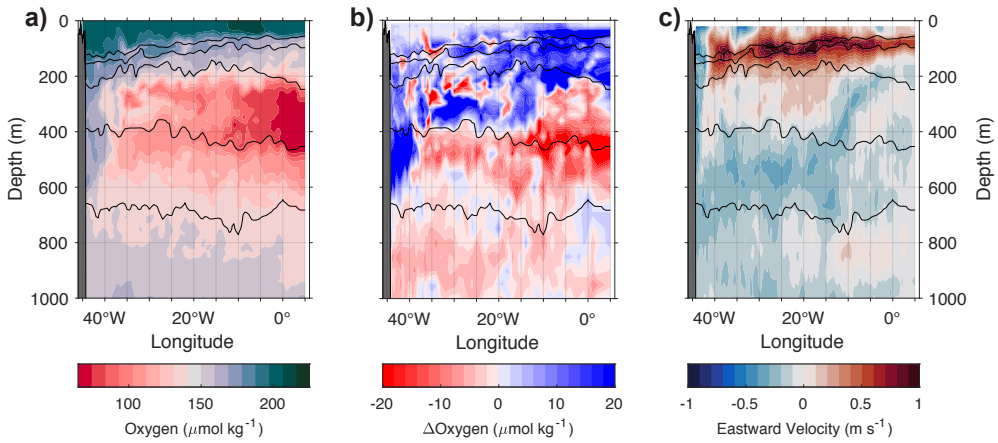

401

402 **Fig. 2 Shipboard measurements along the Atlantic equator in Sep./Oct. 2019. a**, Dissolved
403 oxygen concentration. **b**, Dissolved oxygen anomaly relative to the climatological year-2000
404 state[25]. **c**, Eastward velocity. Grey areas mark bottom topography at the western boundary.
405 Black lines mark the 25 kg m^{-3}, 26 kg m^{-3}, 26.5 kg m^{-3}, 27 kg m^{-3} and 27.25 kg m^{-3} isopycnals.

406

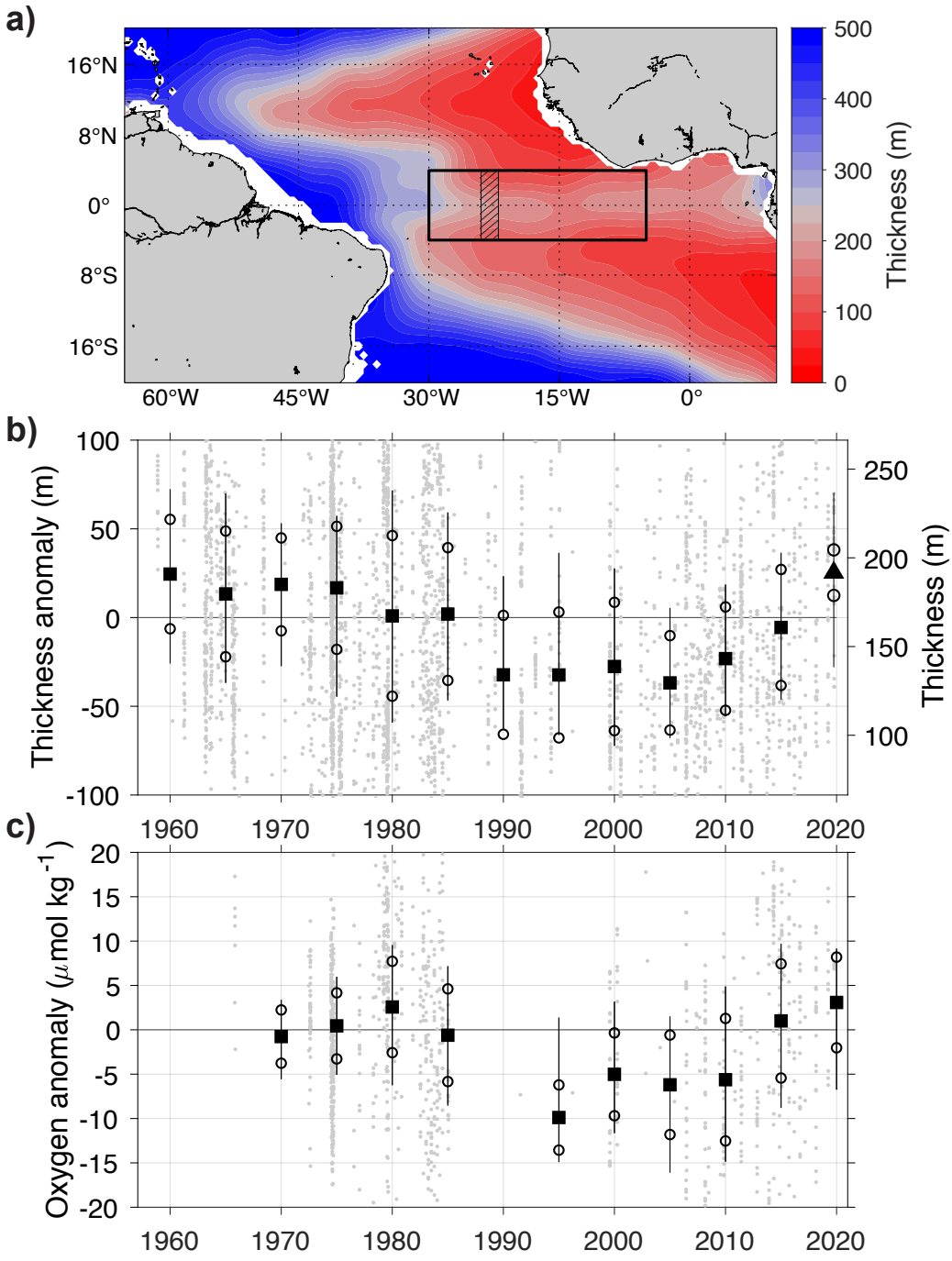

Fig. 3 Surface oxygenated layer thickness (OLT) in the tropical Atlantic. a, Mean OLT. **b**, Time series of OLT anomaly in the equatorial region (35°W-5°W, 4°S-4°N) marked in (**a**). **c**, Time series of the oxygen anomaly in the box 100-200m, 24°W-22°W, 4°S-4°N marked in (**a**) by the hatched area. Indicated in (**b**) and (**c**) are the ten-year median anomalies (black squares),

413 the probable error of the median derived from the median absolute deviation (open circles), as
414 well as the corresponding interquartile range (black lines) of the individual data anomalies (grey
415 dots). The triangle marks the median anomaly of data taken in Sep./Oct. 2019. OLT is defined
416 by the depth range between ocean surface and shallowest depth of the 120 μmol kg^{-1} oxygen
417 surface.

418

Methods

We use different observational datasets from moored and shipboard measurement programs (particularly from cruise TRATLEQ 1, RV Meteor cruise M158 in September/October 2019), different wind products, and historical oxygen data within this study.

Moored velocity data

Velocity data from the equator at 23°W (Fig. 1c) were acquired using moored acoustic Doppler current profilers (ADCPs). They cover the whole depth range of the EUC for most of the 12 to 18 months long consecutive mooring periods except for a few years at the beginning[31]. All velocities were detided using a 40-h low-pass filter and subsampled to 12-h intervals. The oceanic variability on short timescales (i.e. during a single mooring period) clearly exceeds the measurement accuracy of the different instruments. Errors in ADCP compass calibration are expected to be unsystematic for the different instruments used, not able to produce an artificial eastward velocity trend for a ten-year period that encompasses several, typically 1.5-year long mooring periods. Similar trends in northward velocity are substantially smaller and not significant. Moored velocity data from the equator at 10°W were acquired by single upward looking ADCPs. Data treatment was the same as for the 23°W moored velocity data.

EUC transport

For five years as part of the Tropical Atlantic Climate Experiment (TACE), i.e. from mid-2006 to mid-2011, additional moorings were installed at 0°45'N and 0°45'S to obtain a well-defined EUC transport time series. The EUC transport was obtained using variability patterns derived from shipboard observations that were regressed onto the moored time series. Error estimates of these calculations are given as RMS differences[16]. The EUC transport based on three moorings (RMS difference of 0.79 Sv) was used to validate the reconstruction of the EUC transport using only the central mooring (RMS difference of 1.29 Sv), which was the only

mooring operated from mid-2011 onwards[16]. The EUC transport represents the integral of the eastward velocity, u, with u>0 of the reconstructed sections over latitude and depth within the domain covering 30-300 m depth and 1°12'S - 1°12'N. The EUC transport is characterized by substantial intraseasonal variability of 2.3 Sv (standard deviation of 8-to-90-day band-pass filtered data), a seasonal cycle of 1.2 Sv (standard deviation of the monthly mean seasonal cycle), and multiannual variability of 1.1 Sv (standard deviation of detrended time series with annual and semi-annual harmonics subtracted and 270-day low-pass filtered).

To test the sensitivity of the ten-year trend of the EUC transport to the used definition, we have calculated different versions of the EUC transport: Version 1) only positive u, 30-300m and 1°12'S - 1°12'N (as we used in the manuscript), Version 2) positive and negative u, 30-300m and 1°12'S - 1°12'N and Version 3) positive and negative u, 30-200m and 1°S - 1°N. The area in version 3 was reduced in order to avoid most areas with westward velocities. All three versions show a clear increase in the EUC transport (Supplementary Fig. 3). Version 2 shows the strongest intensification, which is due to the fact that areas with westward velocities additionally decrease during EUC intensification. Version 3 shows the smallest increase, which is due to the fact that part of the EUC is missing, when shrinking the area. In summary, the estimated ten-year trend of the EUC transport that we present in the manuscript is more on the conservative side of possible estimates.

Shipboard measurements during TRATLEQ 1

Salinity, temperature, depth, oxygen (CTD-O_2) measurements during TRATLEQ 1 were carried out with a Seabird Electronics (SBE) 9plus system that was equipped, in addition to its own pressure sensor, with two parallel sensor sets for temperature, conductivity, and oxygen (Supplementary Tab. 4). The oxygen measurements were calibrated against Winkler-titrated oxygen from discrete water samples. For the calibration a linear correction polynomial depending on pressure, temperature and the actual oxygen value was fitted. A total of 403

oxygen data points were recorded, which resulted in an RMS-misfit of about 1.1 μmol kg^{-1}. Velocities along the equator during TRATLEQ 1 were measured by two vessel-mounted ADCP systems (Supplementary Tab. 4). A 75-kHz RDI Ocean Surveyor mounted in the ship's hull provided the velocity distribution in the upper 650 m with a vertical resolution of 8 m. The second instrument, a 38-kHz RDI Ocean Surveyor installed in the sea chest, had a measurement range of at least 1000 m at a vertical resolution of 32 m. Both datasets were vertically linearly interpolated on a 10-m grid and then combined with a linear weight transition for 75-kHz : 38-kHz velocities of 5:1 in the upper 350 m depth, 3:1 in the depth range between 350 and 500 m depth and 1:1 below 500 m depth. The combined dataset was then mapped onto a common grid of 0.2° × 10 m resolution using Gaussian mapping scales with a horizontal half width scale of 0.2° and cut-off scale of 0.6° and vertical mapping scales of 8 m for half width and 16 m for cut-off. The data were horizontally linearly interpolated between 2.6°E and 5°E to fill the data gap.

Ekman transport from different wind products

The Ekman transport was calculated from different wind products. The meridional Ekman volume transport per unit length [Sv m^{-1}] is

$$T_{Ek,y} = \frac{\tau_x}{\rho_0 f}$$

with τ_x the eastward wind stress, ρ_0 water density (taken here to be 1025 kg m^{-3}) and f the Coriolis parameter. Following[51], τ_x is calculated using the 10-m wind vector, $\vec{v}_{10}$, and the 10-m eastward wind component, u_{10}

$$\tau_x = \rho_{air} c_D u_{10} |\vec{v}_{10}|$$

with ρ_{air} air density (taken here to be 1.223 kg m^{-3}) and c_D drag coefficient for neutrally stable conditions[52]

491 $$c_D = \left(\frac{2.70}{|\vec{v}_{10}|} + 0.142 + 0.0764|\vec{v}_{10}|\right) \times 10^{-3}$$

492 The meridional Ekman transport [Sv] through 10°N and 10°S was eventually calculated by
493 zonal integration of $T_{Ek,y}$ along the respective latitudes between the western and eastern
494 boundaries. The Ekman divergence [Sv] was calculated as the difference between the
495 meridional Ekman transport through 10°N and 10°S. Annual and semi-annual cycles were
496 calculated for the same period, that was used for the ten-year trend calculation (2008-2018),
497 and subsequently removed from the whole time series. Derived time series were then 270-day
498 low-pass filtered.

499 *Trend calculation and significance*

500 Linear trends presented in this study were obtained from a linear regression of a time series of
501 limited length. The 95% confidence interval was calculated following[53] as product of the
502 estimated standard deviation of the trend and the t-score of the Student's t-distribution for 95%
503 significance and n-2 degrees of freedom, where n is the number of independent values used for
504 the linear regression. n was estimated from the autocorrelation functions for the different time
505 series, which revealed an average decorrelation scale of 6 months for time series with annual
506 and semi-annual cycles removed and 270-day low-pass filtered to remove seasonal and shorter
507 period variability. Hence, the trend calculations were evaluated based on 6-months averages.
508 The trend errors of Ekman transports and divergences do not account for possible biases
509 inherent in the different wind products. However, differences in the trends derived from
510 different wind products provide an estimate of the uncertainty.

511 *Oxygen data and analysis*

512 All used oxygen data are listed in Supplementary Tab. 5. Duplicates were avoided by using the
513 first profile in the combined dataset within 24 h and 5 km to all others. For each used profile

514 the uppermost depth of the 120 μmol kg^{-1} oxygen surface was determined by linear vertical
515 interpolation. The climatological mean state of this oxygen surface was then computed by a
516 least squares model on a 0.5°×0.5° grid. For each grid point to be mapped all data within a
517 radius of 1200 km are used by applying a Gaussian weighting using a half folding width of 275
518 km. Prior to the mapping a linear gradient in latitude and longitude as well as a quadratic fit in
519 latitude was subtracted from the original data. An absolute minimum weight of 0.01 was applied
520 to the Gaussian weighting to take the larger distribution and horizontal gradients of the depth
521 of the 120 μmol kg^{-1} oxygen surface better into account. For each profile the depth anomaly of
522 the 120 μmol kg^{-1} oxygen surface compared to the local climatological mean was derived. All
523 anomalies within the equatorial box (35°W-5°W, 4°S-4°N) were used to derive a monthly
524 median offset. The final temporal OLT (120 μmol kg^{-1} oxygen surface) anomaly was computed
525 by the median of all anomalies within 10 years, corrected by the monthly offset.

526 To verify the statistical significance of the median we compute the median absolute deviation
527 (MAD) as a robust measure of the variability of the sample, in addition to the interquartile
528 range. The probable error of the median as derived from the MAD as provided in Fig. 3b and
529 3c is calculated as follows. The MAD is defined as the median of all deviation from the median.
530 Assuming a normal distribution we get the probable error by multiplying the MAD with 1.4826
531 [54].

532 For a detailed description of the data handling of historical data including the stability of oxygen
533 measurements and the likelihood of systematic biases as well as a verification of the mapping
534 bias the reader is referred to[25]. Modern oxygen data since 2006 are validated by a crossover
535 analysis for all recent data[55]. The accuracy of oxygen data taken during cruises since 2006
536 (Supplementary Tabs. 4 and 6) is estimated to be better than 2 μmol kg^{-1} as derived from the
537 calibration with the Winkler titration method.

538 *Oxygen budget and flushing time*

To provide a more quantitative view on the link between EUC intensification and oxygenation, we specifically focus on the layer between 100 and 200 m depth that contains in most places the mean depth of the 120 μmol kg^{-1} oxygen surface (Fig. 3). Here, we want to provide some bulk estimates for oxygen changes and volume flushing rates. To relate the OLT estimated in the region 35°W-5°W, 4°S-4°N (Fig. 3b) to oxygen changes in the layer 100-200m, it is most convenient to look at the 23°W section, which provides best data coverage (Supplementary Fig. 7). Taking oxygen data presented in Fig. 3c representing the box 100-200m, 24°W-22°W, 4°S-4°N, we find an oxygen decrease of -1.7 ± 0.6 μmol kg^{-1} decade^{-1} for the period 1960-2004 and an oxygen increase of +9.5 ± 1.8 μmol kg^{-1} decade^{-1} for the period 2005-2020. This variability of the subsurface oxygen concentration is in general agreement with the thinning and thickening of the surface oxygenated layer during the corresponding periods found in the region 35°W-5°W, 4°S-4°N (Fig. 3b).

The main oxygen supply to the box 100-200m, 4°S-4°N, 35°W-5°W is via the EUC. However, how much the intensification of the EUC during the period August 2008 to July 2018 did contribute to the oxygen increase depends not only on the EUC inflow, but similarly on the EUC outflow at the eastern boundary of the box, other inflows and outflows such as associated with the different branches of the South Equatorial Current as well as on the remaining terms of the oxygen budget. Formally the volume integrated oxygen budget can be written as follows:

$$\int_V \frac{\partial O}{\partial t} dV = V \frac{\partial O_{Box}}{\partial t} = \oint_{\partial V} (O\vec{u}) \cdot \vec{n} dS + R$$

where V is the box volume, O is oxygen, t is time, O_{Box} is the mean oxygen concentration in the box, $\vec{u}$ is the velocity vector, ∂V is the boundary of the volume and $\vec{n}$ the inward normal vector to ∂V. Mass conservation requires $\oint_{\partial V} \vec{u} \cdot \vec{n} dS = 0$ or the inflow into the box must equal the outflow out of the box. The residuum, R, includes all other budget terms, particularly lateral

562 eddy fluxes, diapycnal mixing, and oxygen consumption that all might change for an
563 intensifying EUC and increasing oxygen concentration.

564 While we have provided an estimate of the temporal change of the mean box oxygen
565 concentration by calculating the oxygen change along ~23°W (Fig. 3c), the other budget terms
566 are largely unknown. However, we can give an estimate of the oxygen supply into the box due
567 to the EUC. For the climatological mean state, we can write the volume integrated oxygen
568 budget as follows:

569 $$0 = \oint_{\partial V} (O_c \vec{u}_c) \cdot \vec{n} dS + R_c$$

570 where O_c is the climatological oxygen concentration, $\vec{u}_c$ is the climatological velocity vector,
571 and R_c is the climatological residuum that balances the oxygen transport divergence in a
572 climatological mean state. Here, we can approximate the mean advective oxygen supply by the
573 climatological EUC as $O_{in}T_0$, where O_{in} is the temporal mean, transport-weighted oxygen
574 concentration of the climatological EUC with transport T_0. An intensification of the EUC would
575 result in a flushing of the box volume with excess EUC waters that, in case of a complete
576 flushing and no other damping terms, would increase the mean box oxygen concentration by
577 $O_{in} - O_{Box,0}$, with $O_{Box,0}$ being the mean oxygen concentration in the box at the time, t_0, when
578 the EUC intensification starts.

579 The flushing time, t_{flush}, can be estimated as

580 $$\int_{t_0}^{t_0+t_{flush}} (T - T_0) dt = V$$

581 where T is the EUC transport. Here, we can only calculate the EUC transport time series at
582 23°W, which is not at the western boundary of our box. However, the EUC at 23°W is a direct
583 continuation of the EUC arriving at 35°W and can serve as a good approximation of the

584 increasing EUC oxygen supply. The transport-weighted mean oxygen concentration of the EUC
585 flow at 23°W, 100-200m, 1.2°S-1.2°N that can be derived from Fig. 1b is 153 μmol kg^{-1}. It is
586 thus substantially higher than the mean oxygen concentration in the box estimated at 23°W,
587 100-200m, 4°S-4°N to be 120 μmol kg^{-1}. The EUC transport at 23°W in that layer before the
588 EUC intensification (averaged between August 2005 and July 2008) is 5.4 Sv (Supplementary
589 Fig. 4a). For the excess transport due to the intensifying EUC, $T - T_0$, a flushing time of the
590 box volume can be estimated to be about 10 years (Supplementary Fig. 4b). Note that the
591 flushing time of the box volume by the climatological EUC transport, T_0, is only 1.7 years. The
592 excess EUC transport is thus strong enough to potentially exchange the whole box volume
593 during about the period of EUC intensification discussed here. However, due to several negative
594 feedback mechanisms, the mean box oxygen concentration will not reach the oxygen level of
595 the inflowing EUC. Among the negative feedback mechanisms are an increasing oxygen
596 concentration of the outflow (that is part of the term $\oint_{\partial V}(O\vec{u}) \cdot \vec{n}dS$) as well as a changing
597 residuum, R. The latter include processes like enhanced lateral oxygen eddy fluxes out of the
598 box and reduced diapycnal oxygen flux into the box from above due to changed lateral and
599 vertical oxygen gradients, respectively, all associated with an increasing mean oxygen
600 concentration in the box. Changes in consumption could occur as well, e.g., associated with an
601 enhanced nutrient supply of the equatorial upwelling by the EUC intensification, enhanced
602 biological production and consequently enhanced consumption due to heterotrophic respiration
603 of sinking biological material. However, these terms of the oxygen budget cannot be
604 meaningfully quantified with the observational data at hand.

605 **Data and code availability**

606 All data supporting the findings of this study are publicly available as referenced within the
607 paper and in the supplementary material (Supplementary Tabs. 1, 4, and 5). All necessary

code for the data analysis and preparation of the figures of this manuscript is freely available at https://doi.org/10.5281/zenodo.4436007.

References

51 Risien, C. M. & Chelton, D. B. A Global Climatology of Surface Wind and Wind Stress Fields from Eight Years of QuikSCAT Scatterometer Data. *J Phys Oceanogr* **38**, 2379-2413, doi:10.1175/2008jpo3881.1 (2008).

52 Large, W. G., Mcwilliams, J. C. & Doney, S. C. Oceanic Vertical Mixing - a Review and a Model with a Nonlocal Boundary-Layer Parameterization. *Rev Geophys* **32**, 363-403, doi:10.1029/94rg01872 (1994).

53 von Storch, H. & Zwiers, F. W. *Statistical Analysis in Climate Research*. (Cambridge University Press, 2001).

54 Rousseeuw, P. J. & Croux, C. Alternatives to the Median Absolute Deviation. *J Am Stat Assoc* **88**, 1273-1283, doi:Doi 10.2307/2291267 (1993).

55 Olsen, A. *et al.* GLODAPv2.2019-an update of GLODAPv2. *Earth Syst Sci Data* **11**, 1437-1461, doi:10.5194/essd-11-1437-2019 (2019).